The importance of graphene stacking sequence in the Li-intercalation mechanism

Pascal Puech, Shaorui Chen, Yuxin Xiang, Tianzhao Hu, Marc Monthioux, Lili Zhang, Feng Li

Research article

Carbon Future

The importance of graphene stacking sequence in the Li-intercalation mechanism

Pascal Puech [1] ✉, Shaorui Chen[2], Yuxin Xiang[2], Tianzhao Hu[2], Marc Monthioux[1], Lili Zhang[2], and Feng Li [2,3] ✉

[1] *Centre d'Elaboration de Matériaux et d'Etudes Structurales, UPR-8011 CNRS, Université de Toulouse, 29 rue Jeanne Marvig, 31055 Toulouse Cedex 4, France*
[2] *Shenyang National Laboratory for Materials Science, Institute of Metal Research, Chinese Academy of Sciences, Shenyang 110016, China*
[3] *School of Materials Science and Engineering, University of Science and Technology of China, Shenyang 110016, China*

Cite This: *Carbon Future* **2024**, *1*, 9200026

Read Online

ABSTRACT: Graphenic materials used as anodes in lithium-ion batteries have the lowest specific capacity at around 2000 °C. Consequently, graphite is predominantly used, and few studies have investigated the intermediate annealing temperature range of 2000 °C. Starting from a graphitizable coke, this study investigates the lithium-intercalation capacity of graphite materials at increasing carbonization temperatures (1700, 2000, 2100, and 2500 °C). The results are correlated with the structural evolution determined via X-ray diffraction (XRD). The variation in Li-intercalation performance is assigned to the evolution of graphene stacking sequences. Intercalation begins during the early stages of graphitization with the appearance of AB pairs (AB stacking sequence), indicating that the mechanism starts even before the formation of the true graphitic structure. The sample carbonized at 2100 °C exhibits the highest concentration of AB pairs of graphenes, approaching 50%. Consequently, electrical characteristics during lithiation/delithiation reveal a marked transition from stage 1/stage 2 to stage 2/stage 2L in turbostratically stacked samples, while more graphitized samples with AB pairs and then graphitic (ABA, etc.) sequences display a stage 2/stage 2L to stage 2L/stage 3 transition. Raman spectroscopy and anode color changes confirm the various stages. This research enhances our understanding of the lithium-intercalation process in graphite materials in relation to the structural composition of the average crystallite.

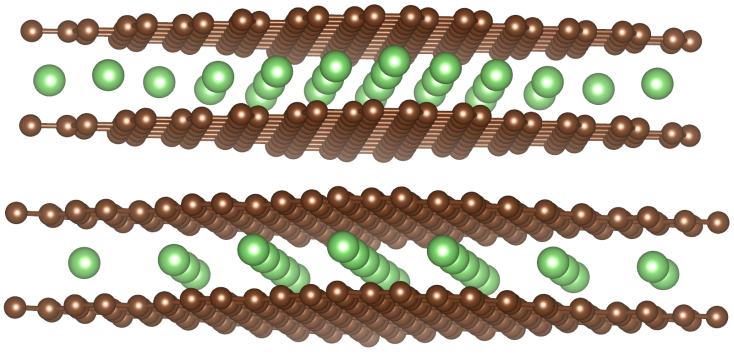

KEYWORDS: intercalation, stacking, Raman, battery

1 Introduction

Graphite exhibits a high lithium intercalation capability with a flat lithium intercalation voltage curve, which is favorable for commercial lithium-ion batteries[1]. Consequently, the differences in the lithium storage mechanism and performance between graphite and other graphenic materials have attracted tremendous interest[2], sometimes coming out with strategies to overcome theoretical graphite specific capacity (SC) with lithium plating[3]. The crystallographic structure of graphenic materials, which determines the intercalation capacity, is controlled by the carbonization (possibly up to graphitization) temperature and the intrinsic graphitizability. It has been reported[4] that the capacity for graphitizable materials obtained by high-temperature carbonization is the largest at both ends of the 1700–2500 °C temperature range but reaches a minimum at around 1800 °C. However, few studies have been devoted to the Li-intercalation behavior in this particular range of temperatures and the underlying causes of the non-linear variations remain unclear.

The intercalation of Li (or K) into graphite shows several stages. Stage 1 is an alternation of 1 carbon layer and 1 intercalate layer. Stage 2 is an alternation of 2 carbon layers and 1 intercalate layer, and so on. Two specific denominations in the case of lithium are "diluted stage 1" (stage 1L), where atoms start to intercalate without forming a specific stage, and likewise for stages 2L, 3L, and so on (where L refers to the liquid-like phase). Li^+ intercalation starts with stage 4 and then with the coexistence of two stages at the same time. This has been explained by energetic and geometric considerations[5]. On the contrary, the intercalation process in non-graphitic graphenic carbons, where turbostratic stacking sequences prevail, is less favorable[4, 5], thus hindering the formation of a higher stage.

Received: November 7, 2024; **Revised:** December 14, 2024
Accepted: December 15, 2024

✉Address correspondence to Pascal Puech, pascal.puech@cemes.fr; Feng Li, fli@imr.ac.cn

https://doi.org/10.26599/CF.2024.9200026

The structural characterization of electrochemically-intercalated graphite compounds as anode materials in lithium-ion batteries covers several techniques[6]. In this study, X-ray diffraction (XRD), potential profiles during intercalation–deintercalation cycling, optical images of the carbon anode, and Raman spectroscopy have been used to characterize the electrochemical intercalation of Li in graphitizable graphenic carbons. These techniques are complementary and have been previously reported for this purpose[6]. The stage coexistence at various temperatures and various charge rates were visible with *in operando* X-ray diffraction[7]. As X-ray diffraction averages over multiple graphene layers[8], possibly hundreds of them, and as the other techniques have their limitations as well, different interpretations of the intercalation mechanisms have been proposed[9]. Anyway, as this work was carried out at room temperature (25 °C), we assume that two consecutive phases can coexist[9].

X-ray diffraction is a widely used technique for characterizing the nanotexture/crystallinity and structure (as defined in Ref.[10]) of the carbon materials investigated. Through the analysis of several characteristic peaks by a bottom-up approach, it is possible to determine the proportions of the three elemental structural components (ESCs) (turbostratic, AB pair, and graphitic stacking) that were found to build the average crystallite[8, 11]. This method refines with much more accuracy and details the standard degree of graphitization only determined from the d_{002} position and proposed in the 1950s[12]. X-ray diffraction is often used to monitor the kinetics of intercalation. By monitoring the interlayer spacing (referred to as d_{002} in the framework of graphite indexation), the intercalation stages can be identified[5, 13]. A high charging rates can be complementarily analyzed by transmission electron microscopy (TEM)[14], which reveals nonequilibrium intercalation and larger spacing than with stage 1.

Several modes in electrochemical measurements are used: the potential (versus Li^+/Li) versus specific capacity, the specific current as a function of the potential (versus Li^+/Li), and the first and second derivatives of these curves[4, 15, 16].

The interpretation of Raman data is more challenging for several reasons. The first reason is the electron–phonon coupling, which affects the position[17] and shape[18] of the bands. The Fano shape is dependent on the excitation energy[19], which is not often reported in the literature. Secondly, the sensitivity of graphenic materials to laser power[18] has the potential to modify the Raman signature, necessitating the utilization of exceedingly low laser power. This presents a challenge as, typically, at stage 1, the Raman intensity is markedly weak[20, 21]. Consequently, when a specimen exhibits spectral characteristics that fit multiple features, it can be suspected that this heterogeneity or inconsistency may be attributed to variations in either the synthesis or the observation conditions[22–24]. Finally, the inhomogeneity of the intercalated compounds requires a statistical approach[24], which is too time-consuming during cycling in an electrochemistry cell.

The intercalation stage can be readily followed by color observation, which is well-known for preparing samples with vapor-phase reaction processes[25]. In the case of lithiation, color change has been used by Shellikeri et al.[26] and Hess et al.[27] to evidence stage changes: Blue color corresponds to stage 2L, red to stage 2, and gold to stage 1. For a Gramax material carbonized at ~ 2000 °C as reported by Fujimoto et al.[28, 29], X-ray and nuclear magnetic resonance (NMR) data show a broadening of signatures (in comparison to graphite) associated with a lower specific capacity. The color after lithiation is orange instead of reaching the golden aspect.

2 Materials, cell assembly, and experiments

2.1 Carbon cokes

In this study, a set of four samples were selected from a well-characterized graphitizable carbons[8], with carbonization temperatures (under an inert atmosphere) of 1700, 2000, 2100, and 2500 °C. This temperature range generated the most important variations regarding the stacking sequence between graphene layers, including several transitions: the apparition of AB pairs, the elimination of the turbostratic sequence, and the apparition of the graphitic sequence. The samples came from a series of coal-tar-pitch-based cokes (GFEC-1). It was provided by the French Carbon Society (SFEC, formerly GFEC) and prepared by Le Carbone Lorraine (now MERSEN) to serve as a reference material for graphitizable carbon materials. The heteroatom content was low (0.05%–0.1%) at 1700 °C and even less for higher annealing temperatures.

2.2 Electrochemical measurements

Electrochemical measurements were carried out using a CR2032 coin-type cell. The working electrodes were prepared by mixing 80 wt.% of the active material, 10 wt.% of acetylene black (Super-P), and 10 wt.% of polytetrafluoroethylene (PTFE) binder dispersed in ethanol resulting in a uniform thin film. The film was dried at 80 °C for 12 h to remove solvent, cut into disks with a diameter of 10 mm, and pressed onto stainless steel mesh to create the electrodes. The mass loading of the working electrodes was 3.0–4.0 $mg{\cdot}cm^{-2}$. A lithium foil with a diameter of 10 mm was used as the counter/reference electrode, glass fiber paper (Whatman) was used as the separator, and 1 $mol{\cdot}L^{-1}$ $LiPF_6$ dissolved in a mixture of ethylene carbonate (EC) and dimethyl carbonate (DMC) (EC/DMC, 1:1 v/v) was used as the electrolyte. The cells were assembled in an argon-filled glove box (H_2O < 0.01 ppm, and O_2 < 0.01 ppm).

2.3 Raman spectroscopy

Raman spectroscopy measurements were performed using a Witec ALPHA300R spectrometer equipped with an excitation wavelength of 532 nm and a laser power of 0.5 mW (measured on the specimen). A long working distance 50× objective was used for signal collection. An accumulation time of 200 s was chosen to obtain an adequate signal-to-noise ratio. The optical images were captured with automatic white-balance correction. The device used for the test was a customized cell with a quartz window, and its internal structure was similar to that of the coin-type cell. The anode was placed under the quartz window for optical observation and tested on an electrochemical workstation (Biologic VSP-300). A current density of 20 to 100 $mA{\cdot}g^{-1}$ was used for the cycle. The *in-situ* Raman spectrometry was carried out after the initial discharge and charge process.

2.4 XRD

The XRD experimental diffractograms were recorded on a Bruker D8 advance diffractometer equipped with a Cu Kα radiation source and a Lynxeye 1 D detector using a Bragg–Brentano setup. The specimens were analyzed as powders with a thickness of 0.5 mm on

a zero-background specimen holder to reduce the probability of preferred orientations. The primary divergence slit aperture was fixed at 0.5°. The XRD diffractograms were recorded in a 2θ range between 10° and 90° with a 0.01° step in continuous mode. Diffractograms were analyzed by a bottom-up method we described elsewhere[8]. Briefly, it consisted of

(1) Identifying the various possible ESCs of the average crystallite (here: (i) individual graphenes turbostratically stacked, (ii) pairs of graphenes stacked according to the AB sequence of graphite, and (iii) n graphenes stacked according to the ABA, etc. sequence of the graphitic structure, with $n \geq 3$);

(2) Making atomistic models for each ESC;

(3) Calculating the diffraction profile for each ESC atomistic model;

(4) Parametrizing the functions for fitting the various peaks in the calculated diffraction profiles for each ESC;

(5) Combining the parametrized functions related to each peak of each ESC profile to fit the experimental peaks of the average crystallite;

(6) Leaving as far as possible our lab-developed software free to adjust the critical parameters (L_a, L_c, L_c', number of graphitic entities, and the proportions of each ESC) to fit the experimental diffraction profiles at best.

In item (6) above, the "graphitic entities" are the portions of the average crystallite in which the graphenes are stacked according to the graphitic sequence. L_c' corresponds to the average height (related to the number of graphenes involved combined with 0.335 nm as the inter-graphene distance) of these graphitic entities. Both L_c' and the proportion of the various ESCs are new parameters only accessible via our bottom-up approach.

3 Results

3.1 XRD

The X-ray diffractograms of the set of samples are shown in Fig. 1, with selected ranges of 2θ diffraction angle displayed separately so that proper magnification and angle scale could be used for each of them to enhance the important features. The 23°–28° range (Fig. 1a) shows the gradual shift with increasing temperature of the 002 peak which marks the progressive decrease in the average intergraphene distance in the average crystallite. The 40°–65° range (Fig. 1b) shows the progressive change of the 10(0)/101 peak profiles with increasing temperature: The 10 peak is first asymmetric because of the turbostratic structure, then the AB pairs show up (creating a bump (arrowed)), then the occurrence of the graphitic stacking brings more symmetry to the peaks. The 75°–90° range (Fig. 1c) shows similar events as the previous range, with another signature of AB pairs (arrowed) occurring also for the 2100 °C-coke sample.

In previous works, we have reported the fit of the diffractograms over the whole 2θ range[8, 11]. The extracted parameters are presented in Table 1, and the fits are shown in the Supplementary Figs. S2–S5. This set of samples is representative of the graphitization process going from 1700 °C with no detectable AB pair (100% turbostratic only) to 2500 °C, which contains a majority of graphitic stacking in addition to AB pairs, with no single layer turbostratically-stacked left. As a validation of our bottom-up methodology and of the values obtained. L_a determined from 10(0) and 11(0) exhibits similar values (L_{a10} is more accurate at intermediate temperatures with our approach) except for annealing at 2500 °C, where stacking faults (rhombohedral sequences) broaden the apparent 100 peak leading to a lower L_{a10}, while not affecting the 110 peak[11]. Therefore, only the L_{a11} is reliable at high temperatures[11]. The sample annealed at 2100 °C has the largest proportion of AB pairs and has been selected for further optical observation. Meanwhile, the L_{a11} value increases continuously with the increasing temperature.

3.2 Potential and second derivative

A coin cell was employed to analyze the lithiation and delithiation processes through variations in cell potential at a current density of 20 mA·g^{-1}. With the 2100 °C-coke, the inflection points on the curve are visible in Fig. 2a. Consequently, we have identified the features by considering the second derivative of the curve and plotting it as a function of the potential. This corresponds to Figs. 2b and 2c. Two peaks appear when delithiating the intercalated

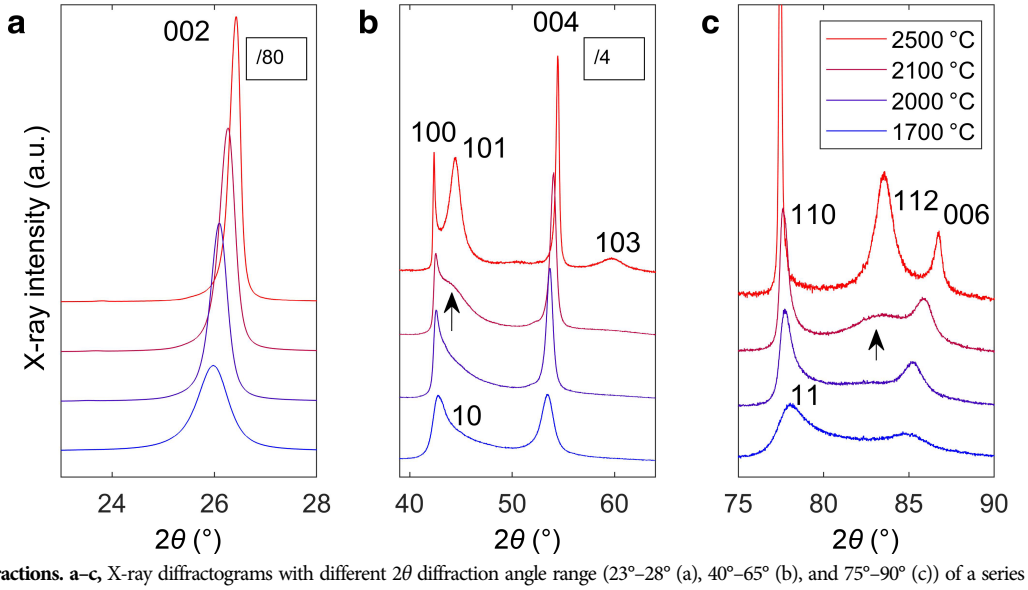

Fig. 1. X-ray diffractions. a–c, X-ray diffractograms with different 2θ diffraction angle range (23°–28° (a), 40°–65° (b), and 75°–90° (c)) of a series of pitch cokes with carbonization temperatures of 1700, 2000, 2100, and 2500 °C, respectively. The arrows indicate the specific signature of AB pairs. Each box corresponds to a different 2θdiffraction angle range, in which the magnification for the left and middle ones has been reduced concerning the right one by the factor indicated in the insets.

compound. The first one, between 0.05 and 0.13 V, is associated with the transition from stage 1/stage 2 to stage 2/stage 2L. The second is associated with the transition from stage 2/stage 2L to stage 2L/stage 3 according to Refs.[13, 30]. During lithiation, these features are not visible except for the sample annealed at 2500 °C. It can be noted that the two features are distinctly visible in the 2100 °C-coke. In a previous study, Fujimoto[4] reported the intercalation of Li however without forming higher stages (i.e., 3 or more).

The 2500 °C coke exhibits no discernible turbostratic stacking and the specific capacity during loading increases without inflection in the region below 0.2 V (Figs. 2b and 2c). This is consistent with the thermodynamical analysis conducted by Reynier et al.[31]. The number of intercalation sites in the sample carbonized at high temperatures (2500 °C, hence close to graphite) is observed to increase[31]. Two distinct modes of lithium intercalation can be considered, a minor one corresponding to spreading intercalation energies for random transition between graphitic components and the predominant one with a well-marked transition for graphitic components. During the charging process, the well-marked transition from stage 1/stage 2 to stage 2/stage 2L in Fig. 2b is dependent on the number of turbostratically-stacked individual layers in the average crystallite. This is marked for the sample containing the maximum of AB pairs (at 2100 °C), meaning that, as the turbostratic layers are statically surrounded (within the crystallite) by AB pairs, the energy spreading is no longer possible.

The specific reversible capacity of the 2000 and 2100 °C cokes are 240.8 and 274.4 mAh·g^{-1}, respectively (third cycle out of 5 cycles with the specific current density of 20 mA·g^{-1}, with a negligible irreversible contribution). The number of AB pairs is 24% for the former, and 54% with 14% of ABA tri-layers for the latter. The increase in the number of crystallite components having their graphene layers involved in AB stacking (pairs, triplets, and more) is associated with an increase in the specific capacity. This is potentially related to the possibility of Li being intercalated in a specific site with minimum energy and suitable (periodic) atomic organization.

The specific capacity is plotted as a function of the annealed temperature in Fig. 3, along with other results from the literature. According to Reynier et al.[31], at low carbonization temperatures (i.e., lower than 100–1200 °C), the lithium insertion occurs into a variety of sites with a wide distribution of energies whereas, at high temperatures, the chemical intercalation is different, in a more limited number of sites with a three-dimensional organization. The presence of heteroatoms such as hydrogen correlates well with the

Table 1 Parameters deduced from the fit of the experimental diffractograms reported in Fig. 1. Data obtained from 10(0) (L_{a10} and %AB-pair$_{10}$) are provided for information, but from 2500 °C they have to be discarded and data from 11(0) have to be considered instead because the former is much more biased by the presence of stacking faults than the latter. (*): The stacking faults should be taken into consideration in the determination from 10(0), but it is not necessary for 11(0)[11]

Coke	L_{a10} (nm)	L_{a11} (nm)	L_c (nm)	d_{002} (nm)	Turbostratic (%)	AB-pair$_{10}$ (%)	AB-pair$_{11}$ (%)	Graphitic (%)
1700 °C	7.7	6.4	10.3	3.43	100	0	0	0
2000 °C	16.7	17.1	19	3.416	66	34	24	0
2100 °C	24.2	25.9	21	3.395	30	55	54	14 (3 layers)
2500 °C	37	56	30.5	3.366	0	54(*)	35	46 (6 layers)

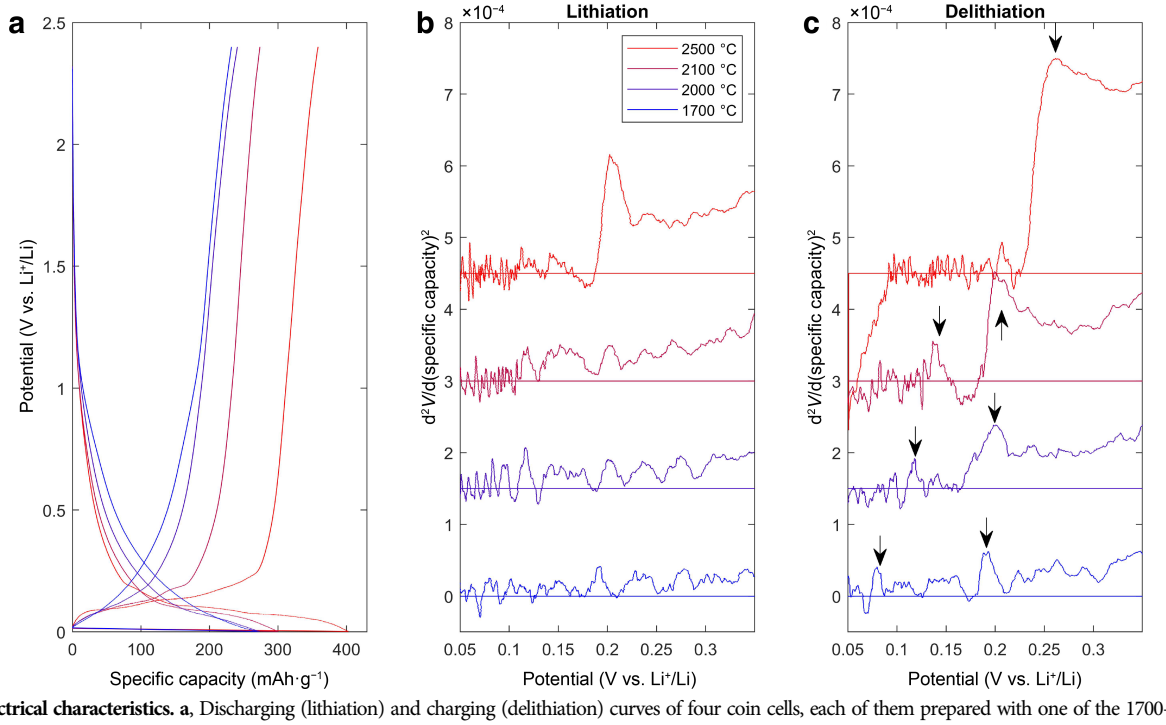

Fig. 2. Electrical characteristics. a, Discharging (lithiation) and charging (delithiation) curves of four coin cells, each of them prepared with one of the 1700–2500 °C-coke series. **b**, Second derivative of the discharge curves. **c**, Second derivative of the charge curves (shifted for clarity). Arrows indicate maxima. The lines serve as visual guides corresponding to zero.

increase of the specific capacitance at low temperatures. The increase of the specific capacity near 0 V versus Li/Li$^+$ is due to unorganized carbon sites (the other storage site for lithium, in addition to layer sites) allowing overcoming the theoretical value of graphite[32].

3.3 Optical image and Raman spectroscopy

For the sample containing the largest number of AB pairs (2100 °C-coke), an optical cell was used to follow the typical Raman spectra and the color of the carbon anode. This aimed at a more comprehensive understanding of the role of the AB pairs. The G band is the well-known Raman feature corresponding to optical phonons at the center of the Brillouin zone. The D band is activated by defects, while its overtone, the 2D band, does not require defects. Both are due to double resonance processes[34]. In the case of graphite intercalated compounds, it is known that the optical mode (mixture of G mode with intercalant) is usually coupled with electrons[17], giving rise to a Fano shape for some excitation conditions.

Figure 4 shows the optical images at different potentials during the intercalation and deintercalation processes for the 2100 °C-coke.

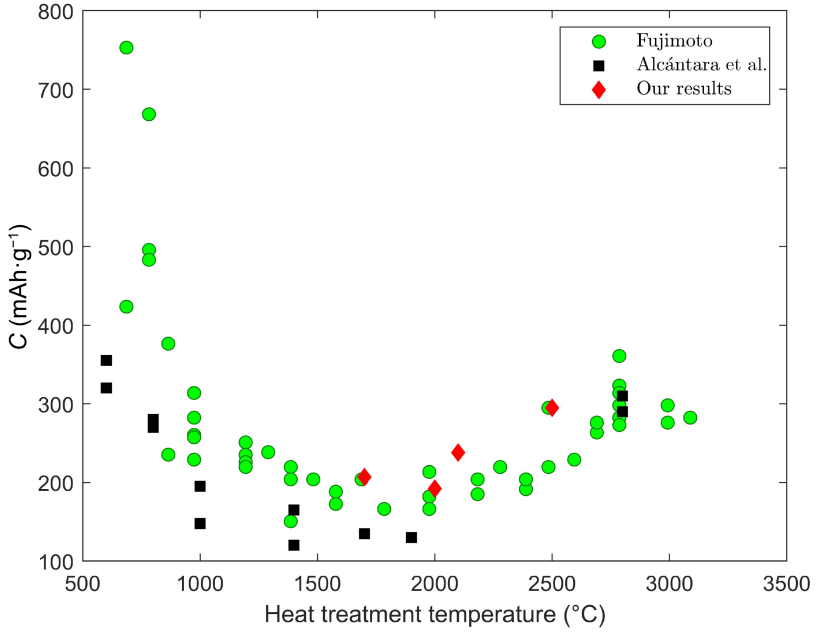

Fig. 3. Specific capacities as a function of annealing carbon temperature. Reversible capacity of the lithium cells versus the carbonization temperature of various carbon materials from Fujimoto[4] and Alcántara et al.[33], along with the cokes from our study.

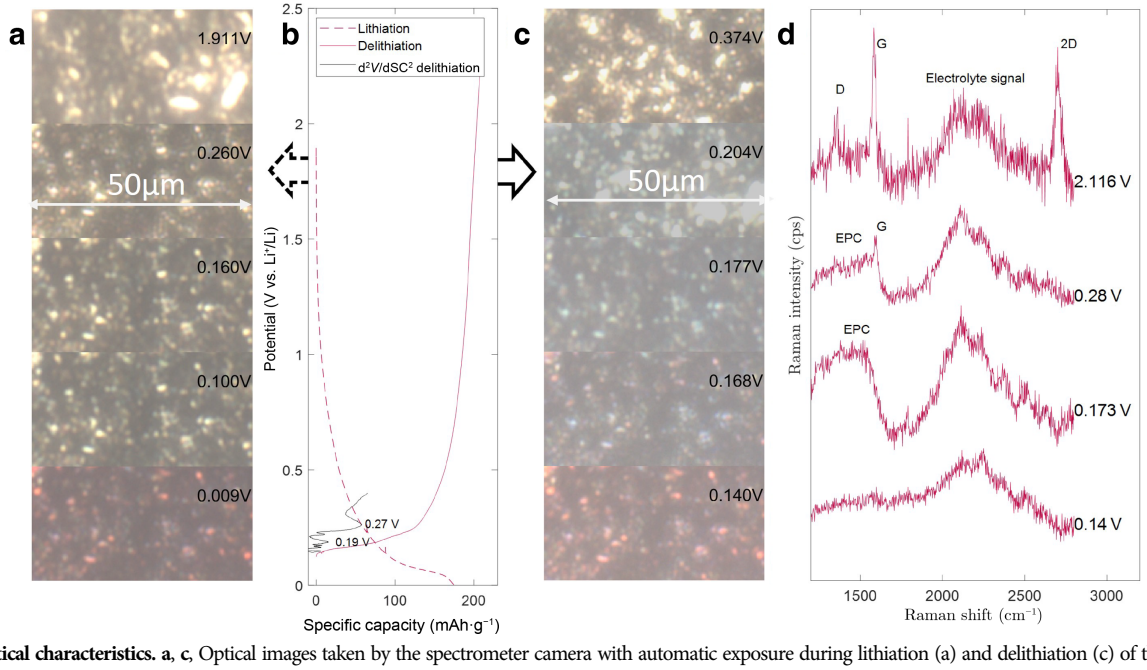

Fig. 4. Optical characteristics. a, **c**, Optical images taken by the spectrometer camera with automatic exposure during lithiation (a) and delithiation (c) of the 2100 °C-coke at increasing positive and negative potential, respectively. **b**, Corresponding plots show the related variation of the specific capacity; the current is 100 mA·g^{-1}, and the curves correspond to the sample pre-cycled twice before a first *in-situ* Raman measurements. **d**, Typical Raman spectra at various potentials during delithiation. The G and 2D phonons are present for crystallized sp^2 carbon, D is activated by in-plane defects, and EPC stands for electron–phonon coupling modes with here a Fano shape.

At the minimum potential, the color transitions to metallic-red, which is characteristic of stage 2 (a small amount of stage 1 is possible). Upon deintercalation, at 0.168 V, red and blue colored areas coexist as a mosaic, corresponding to stages 2 and 2L, respectively[27]. The Raman spectra corresponding to a red (0.14 V) and a blue flake (0.173 V) are shown in Fig. 4d. The geometry of the cell, with the anode located at some distance from the cathode (instead of face-to-face), results in the incomplete attainment of stage 1, attested by the lower specific capacity. The Fano shape is more intense for the blue flake (stage 2L) in comparison to the red one (stage 2). Further deintercalation should be revealed by the occurrence of a narrow peak at 1,580 cm^{-1}, indicating that the graphene layers have deintercalated. This is what is observed from ~ 0.28 V of delithiation tension, for which the G band starts being recovered (Fig. 4d). At the end of the deintercalation process (at 2.12 V), the G and 2D bands of the pristine carbon are almost fully recovered (top spectrum in Fig. 4d). Because a low laser power (0.5 mW) with the 50× objective was used, the risk of deintercalation induced by the laser light previously reported[18] is eliminated. The Raman spectra in Fig. 4d are representative of the various stages, i.e., with the majority of the spectra corresponding to stage 2 for 0.14 V (probably comprising a small proportion of stage 1), stage 2/stage 2L for 0.173 V, and a higher stage (potentially 3) for 0.28 V.

4 Discussion

The occurrence of lithiation has been confirmed through optical and Raman spectroscopy, as well as the characteristic features of the potential versus specific capacity plot (see Fig. 2). For the 2100 °C-coke, the number of AB pairs has become large, and the number of consecutive turbostratically-stacked individual layers has decreased (Table 1). This indicates that the intercalation energy resulting from the sites related to random stacking has become low, due to the disappearance of such random stacking. This leads to two features in the second derivative of the specific capacity versus potential discharge curve (Fig. 2b). In particular, transitions from stage 1/stage 2 to stage 2/stage 2L and from stage 2L to stage 3 are distinctly evident. In comparison to the 1700 °C-coke (which is purely turbostratic) and the 2000 °C-coke (which contains some AB pairs), the specific capacity starts to increase only with the 2100 °C-coke. The lateral size $L_{a11(0)}$ of the crystallites is larger (26 nm at 2100 °C), but in comparison to the change between 1700 and 2000 °C (from 7 to 17 nm), this is not the origin of the observed increase. For the 2500 °C-coke, the proportion of pure-turbostratic structure is zero, and the specific capacity is the largest of the 4 samples. The number of layers (each 0.335 nm thick) in entities with graphitic stacking in the crystallite is larger for this sample (6 for each entity, on average). It should be noted that the related average crystallite (~ 30 nm high) is therefore typically composed of 15 6-layer graphitic entities randomly (= turbostratically) stacked on each other, indicating that this is not the most optimized configuration.

Therefore, it can be summarized from the aforementioned findings that:

(1) As soon as the turbostratic stacking is no longer the only elemental structural component involved in the average crystallite, the specific capacity is not significantly dependent on the crystallite lateral size L_a in the range of 15 to 30 nm. The decrease of the specific capacity due to larger L_a in turbostratic stacking is compensated by the occurrence of graphite-like stacking sequences (AB or ABA, etc.) which have an opposite behavior, i.e., an increase of the specific capacity. This confirms that the intercalation sites for turbostratic carbons and AB-stacking-containing carbons are different in nature.

(2) The number of AB pairs and ABA, etc. graphitic stacking is the key to determining the capacity of annealed graphenic carbon materials once the graphitization process has started. Usually, the degree of graphitization is used to correlate with the capacity, but it does not discriminate between the various stacking sequences in the average crystallite, which allows sorting between the roles of each concerning the intercalation capability. Quantifying the proportions of AB pairs allows proving that if the turbostratic stacking only involves 2 layers, the spreading of the intercalation energy is reduced, giving an inflection to the charge and discharge curves (better-defined peak in Fig. 2c). It is demonstrated that even the only occurrence of AB pairs is sufficient to start to exhibit the behavior of genuine graphite. As opposed to what happens in the pure-turbostratic domain (temperatures below 2000 °C in Fig. 3), the crystallite in-plane size no longer plays a role (whereas it was inversely correlated to the capacity in the turbostratic domain), and the intercalation can be efficient whatever the crystallite in-plane size. In this regard, the 2000 °C-coke is interesting because it is at a transition temperature where both turbostratic and AB stacking sequences coexist in the average crystallite, hence with the same L_a. Despite this, the capacity does not increase for the 2000 °C-coke. It demonstrates that perfect graphenes stacked with perfect parallelism are not the key combination to achieve high intercalation capability. From this transition temperature, an ordered (coherent) stacking is required, possibly to allow the formation of a periodic network of the intercalant.

(3) For turbostratic stacking, a transition to stages higher than 2L is no longer visible on the curve potential versus specific capacity. Thus, we conclude that the Li intercalation in a stage higher than 2L is not favorable.

These findings are consistent with the literature: Fujimoto[4] explained that high stages are not formed with turbostratic stacking in samples annealed at around 2000 °C. Zheng et al.[13] showed that the stacking disorder reduces the capacity independently of the lateral crystallite size L_a. Thermodynamically, Reynier et al.[31] reported that the intercalation sites have a wide range of distribution energies for turbostratic stacking while all the sites are similar for graphite. However, only the turbostratic stacking sequence and the graphitic stacking sequence have been considered so far. Our results extend them to the case of the first step of the occurrence of the graphitic structure which starts with the occurrence of AB pairs only, thereby forming an alternate of turbostratic and AB pair stackings within the average crystallite.

5 Conclusions

This study demonstrates that the mere occurrence of pairs of graphene layers stacked according to the AB sequence (AB pairs), as the initial step of graphitization, can promote lithium intercalation as in graphite, even before the genuine graphitic structure has formed, as evidenced by XRD and the second derivative of the charge–discharge curves. Even AB stacking in graphene pairs can transition from stage 2/stage 2 L to higher stages upon lithium intercalation, significantly enhancing the lithium intercalation capacity. In contrast, the inability of turbostratic stacking to undergo further transition at high stages is not conducive to capacity. The ability of AB pairs to intercalate Li is the

phenomenon that compensates then overcomes, as the carbonization temperature increases, the loss of capacity due to the increase in L_a for crystallites where the turbostratic stacking prevails. As the number of successive turbostratic layers in the average crystallite lowers (due to the occurrence then increasing proportions of AB pairs and ABA, etc. sequences), the spreading of the intercalation energy is reduced. Raman spectra, through a huge electron–phonon coupling, attest the homogeneity of the intercalation, which is further corroborated by the color of the carbon anode. A geometrical consideration, with the possibility of Li being inserted within the AB pair to continue the energy storage by a shift to AA stacking as in graphite[34], is an interesting idea to explore.

References

[1] Li, Y.; Liu, K. L.; Foley, A. M.; Zülke, A.; Berecibar, M.; Nanini-Maury, E.; Van Mierlo, J.; Hoster, H. E. Data-driven health estimation and lifetime prediction of lithium-ion batteries: A review. *Renew. Sustain. Energy Rev.* **2019**, *113*, 109254.

[2] Cao, B.; Du, M. J.; Guo, Z. R.; Liu, H.; Yan, C.; Chen, A. B.; Chen, X.; Tang, C.; Huang, J. Q.; Zhang, Q. The future of carbon anodes for lithium-ion batteries: The rational regulation of graphite interphase. *Carbon Future* **2024**, *1*, 9200017.

[3] Cai, W. L.; Yan, C.; Yao, Y. X.; Xu, L.; Chen, X. R.; Huang, J. Q.; Zhang, Q. The boundary of lithium plating in graphite electrode for safe lithium-ion batteries. *Angew. Chem., Int. Ed.* **2021**, *60*, 13007–13012.

[4] Fujimoto, H. Development of efficient carbon anode material for a high-power and long-life lithium ion battery. *J. Power Sources* **2010**, *195*, 5019–5024.

[5] Zheng, T.; Reimers, J. N.; Dahn, J. R. Effect of turbostratic disorder in graphitic carbon hosts on the intercalation of lithium. *Phys. Rev. B* **1995**, *51*, 734–741.

[6] Li, N.; Su, D. *In-situ* structural characterizations of electrochemical intercalation of graphite compounds. *Carbon Energy* **2019**, *1*, 200–218.

[7] Schmitt, C.; Kube, A.; Wagner, N.; Friedrich, K. A. Understanding the influence of temperature on phase evolution during lithium-graphite (de-)intercalation processes: An *operando* X-ray diffraction study. *ChemElectroChem* **2022**, *9*, e202101342.

[8] Puech, P.; Dabrowska, A.; Ratel-Ramond, N.; Vignoles, G. L.; Monthioux, M. New insight on carbonisation and graphitisation mechanisms as obtained from a bottom-up analytical approach of X-ray diffraction patterns. *Carbon* **2019**, *147*, 602–611.

[9] Allart, D.; Montaru, M.; Gualous, H. Model of lithium intercalation into graphite by potentiometric analysis with equilibrium and entropy change curves of graphite electrode. *J. Electrochem. Soc.* **2018**, *165*, A380–A387.

[10] Monthioux, M. Describing carbons. *Carbon Trends* **2024**, *14*, 100325.

[11] Puech, P.; Jeanningros, M.; Neumeyer, D.; Monthioux, M. Addressing the effect of stacking faults in X-ray diffractograms of graphite through atom-scale simulations. *Carbon Trends* **2023**, *13*, 100311.

[12] Franklin, R. E. The structure of graphitic carbons. *Acta Cryst.* **1951**, *4*, 253–261.

[13] Zheng, T.; Dahn, J. R. The effect of turbostratic disorder on the staging transitions in lithium intercalated graphite. *Synth. Met.* **1995**, *73*, 1–7.

[14] Li, N.; Sun, M. Z.; Hwang, S.; Li, S.; Zhao, H. Y.; Du, Y. P.; Huang, B. L.; Su, D. Non-equilibrium insertion of lithium ions into graphite. *J. Mater. Chem. A* **2021**, *9*, 12080–12086.

[15] Markovsky, B.; Levi, M. D.; Aurbach, D. The basic electroanalytical behavior of practical graphite-lithium intercalation electrodes. *Electrochim. Acta* **1998**, *43*, 2287–2304.

[16] Dahn, J. R. Phase diagram of Li_xC_6. *Phys. Rev. B* **1991**, *44*, 9170–9177.

[17] Saitta, A. M.; Lazzeri, M.; Calandra, M.; Mauri, F. Giant nonadiabatic effects in layer metals: Raman spectra of intercalated graphite explained. *Phys. Rev. Lett.* **2008**, *100*, 226401.

[18] Nemanich, R. J.; Solin, S. A.; Güerard, D. Raman scattering from intercalated donor compounds of graphite. *Phys. Rev. B* **1977**, *16*, 2965–2972.

[19] Tristant, D.; Wang, Y.; Gerber, I.; Monthioux, M.; Pénicaud, A.; Puech, P. Optical signatures of bulk and solutions of KC_8 and KC_{24}. *J. Appl. Phys.* **2015**, *118*, 044304.

[20] Migge, S.; Sandmann, G.; Rahner, D.; Dietz, H.; Plieth, W. Studying lithium intercalation into graphite particles via *in situ* Raman spectroscopy and confocal microscopy. *J. Solid State Electrochem.* **2005**, *9*, 132–137.

[21] Inaba, M.; Yoshida, H.; Ogumi, Z.; Abe, T.; Mizutani, Y.; Asano, M. *In situ* Raman study on electrochemical Li cintercalation into graphite. *J. Electrochem. Soc.* **1995**, *142*, 20–26.

[22] Eklund, P. C.; Dresselhaus, G.; Dresselhaus, M. S.; Fischer, J. E. Raman scattering in graphite-lithium intercalation compounds. *Phys. Rev. B* **1980**, *21*, 4705–4709.

[23] Chacón-Torres, J. C.; Ganin, A. Y.; Rosseinsky, M. J.; Pichler, T. Raman response of stage-1 graphite intercalation compounds revisited. *Phys. Rev. B* **2012**, *86*, 075406.

[24] Wang, Y.; Puech, P.; Gerber, I.; Pénicaud, A. Resonant Raman scattering of graphite intercalation compounds KC_8, KC_{24}, and KC_{36}. *J. Raman Spectrosc.* **2014**, *45*, 219–223.

[25] Enoki, T.; Suzuki, M.; Endo, M. *Graphite Intercalation Compounds and Applications*; Oxford University Press: Oxford, 2003.

[26] Shellikeri, A.; Watson, V.; Adams, D.; Kalu, E. E.; Read, J. A.; Jow, T. R.; Zheng, J. S.; Zheng, J. P. Investigation of pre-lithiation in graphite and hard-carbon anodes using different lithium source structures. *J. Electrochem. Soc.* **2017**, *164*, A3914–A3924.

[27] Heß, M.; Novák, P. Shrinking annuli mechanism and stage-dependent rate capability of thin-layer graphite electrodes for lithium-ion batteries. *Electrochim. Acta* **2013**, *106*, 149–158.

[28] Fujimoto, H.; Yamaki, T.; Shimoda, K.; Fujinami, S.; Nakatani, T.; Kano, G.; Kawasaki, M.; Ogumi, Z.; Abe, T. Phase diagram of Li-graphite intercalation compound formed by the charge/discharge reaction in Li-ion battery. *J. Electrochem. Soc.* **2022**, *169*, 070507.

[29] Fujimoto, H.; Shimoda, K.; Murakami, M.; Kiuchi, H.; Takagi, S.; Kano, G.; Kawasaki, M.; Ogumi, Z.; Abe, T. In-plane ordering of Li-intercalated turbostratic graphite for the negative electrode of high-power long-life Li-ion batteries. *J. Electrochem. Soc.* **2023**, *170*, 060534.

[30] Hess, M. Kinetics and stage transitions of graphite for lithium-ion batteries. Ph.D. Dissertation, ETH Zurich, Zurich, Switzerland, 2013.

[31] Reynier, Y.; Yazami, R.; Fultz, B.; Barsukov, I. Evolution of lithiation thermodynamics with the graphitization of carbons. *J. Power Sources* **2007**, *165*, 552–558.

[32] Takami, N.; Satoh, A.; Ohsaki, T.; Kanda, M. Lithium insertion and extraction for high-capacity disordered carbons with large hysteresis. *Electrochim. Acta* **1997**, *42*, 2537–2543.

[33] Alcántara, R.; Mateos, J. M. J.; Tirado, J. L. Negative electrodes for lithium- and sodium-ion batteries obtained by heat-treatment of

petroleum cokes below 1000 °C. *J. Electrochem. Soc.* **2002**, *149*, A201–A205.

[34] Lenchuk, O.; Adelhelm, P.; Mollenhauer, D. New insights into the origin of unstable sodium graphite intercalation compounds. *Phys. Chem. Chem. Phys.* **2019**, *21*, 19378–19390.

Data availability

All data required to support the conclusions of this paper are included in the manuscript and the Supplementary Information. Further data related to this research can be requested from the corresponding authors.

Acknowledgements

P.P. was supported by a mobility scholarship of the grant NanoX n° ANR-17-EURE-0009 in the framework of the "Programme des Investissements d'Avenir". Agnieszka Dabrowska (University of Warsaw, Poland) is thanked for carrying out the XRD on the cokes at CEMES.

Author contributions

P.P. and F.L. designed the experiments; S.C., P.P., and Y.X. performed the experiments. All authors discussed the experiments and results, and prepared the manuscript.

Competing interests

The authors declare that they have no competing interests.

Additional Information

Supplementary Information The online version contains supplementary material available at https://doi.org/10.26599/CF.2024.9200026.